Optics Letters

Cluster-induced non-topological robust boundary states in a photonic lattice

Jiarui Wang,[1] Junhao Yang,[1] Yixuan Fu,[1] Danning Liu,[1] Kaiwen Ji,[2] Ping Guo,[1] and Xinyaun Qi[1,*]

[1]School of Physics, Northwest University, Xi'an 710127, China
[2]Laboratoire Photonique Numérique et Nanosciences, Institut d'Optique d'Aquitaine, Université Bordeaux, CNRS, Talence, France
*qixycn@foxmail.com

Received 1 January 2026; revised 2 February 2026; accepted 16 February 2026; posted 17 February 2026; published 6 March 2026

In conventional topological photonic lattices, the robustness of boundary states is guaranteed by quantized topological invariants. However, this protection mechanism fundamentally depends on the topological phase of the system, making dynamic reconfiguration difficult. In this work, we introduce three auxiliary lattice sites to the left lattice point of a Su–Schrieffer–Heeger (SSH) lattice, treating the resulting four-atom structure—composed of the left lattice point and the auxiliary sites—as a rotatable cluster. This forms a cluster-doped SSH lattice system. By continuously tuning the cluster rotation angle, we modulate the coupling strength between the clusters and the substrate lattice, thereby enabling on-demand control of boundary states. Our findings reveal that the robustness of the boundary modes is co-determined by the cluster rotation angle and the boundary geometry, with their degree of localization showing a positive correlation with robustness—a behavior distinct from conventional global topological protection. This work establishes a geometry-driven paradigm for boundary-state manipulation, opening new pathways toward programmable and dynamically reconfigurable photonic circuits.

https://doi.org/10.1364/OL.589010

Photonic lattices—artificially fabricated periodic structures—have become a canonical platform for exploring wave physics and for steering light at the micro-scale [1]. By engineering their band structures to emulate various electronic systems, these lattices enable the observation of a rich array of physical phenomena, including discrete diffraction [2], Anderson localization [3], and topological insulation [4]. These advances were not merely academic: the same dispersion-tailoring tools that create Dirac cones [5] or flat bands [6] also enable slow-light buffering [7], directional routing [8], and robust lasing [9], all within a small crystal or a tiny chip. In other words, the versatility of photonic lattices lies in their ability to translate abstract solid-state concepts into immediate device functionality [10].

Among the numerous physical phenomena that have been explored, topological insulators have garnered significant attention due to their distinctive potential in realizing disorder-immune light transport [11].

By simulating the Su–Schrieffer–Heeger (SSH) model [12] and its two-dimensional topological insulator counterparts, researchers have successively observed linear Shockley-type surface states and highly robust two-dimensional topological boundary states [13,14]. It is important to note that introducing rotational or torsional degrees of freedom into SSH-like lattice units and valley-Hall systems has been recognized as an effective approach for constructing boundary and corner states [15]. The core origin of such robustness lies in quantized topological invariants, which typically rely on the protection of global symmetries such as chiral symmetry, inversion symmetry, and so forth. [16]. It should be emphasized that breaking certain protective symmetries may destabilize the corresponding topological phases; However, in other contexts, the deliberate breaking of specific symmetries can instead be a prerequisite for generating novel topological phenomena. Nevertheless, in photonic topological platforms based on symmetry protection, the robustness of boundary states is generally highly sensitive to symmetry breaking. This makes it challenging to achieve flexible dynamic tuning and reconfiguration for photonic devices that rely on topological phases to realize robust boundary states [17], thereby driving the urgent search for alternative mechanisms capable of overcoming these limitations.

Recent pioneering efforts suggest that robust localization can indeed arise from alternative mechanisms. For instance, carefully designed geometric configurations can create boundary potentials that effectively trap waves [18], while non-Hermitian effects related to gain/loss or non-reciprocal coupling can lead to exotic localized states insensitive to certain disorders [19]. Furthermore, nonlinear tuning has been shown to enable controllable localization and delocalization of boundary states across multiple band gaps without relying on quantized topological invariants [20]. These approaches hint at a broader paradigm where robustness is governed by designable parameters rather than immutable topological numbers.

In this work, we introduce three auxiliary lattice sites to the left lattice point of a SSH lattice, treating the resulting four-atom structure—composed of the left lattice point and the auxiliary sites—as a rotatable cluster. This forms a cluster-doped SSH lattice system. By adjusting the boundary geometry and cluster rotation angle, we achieve

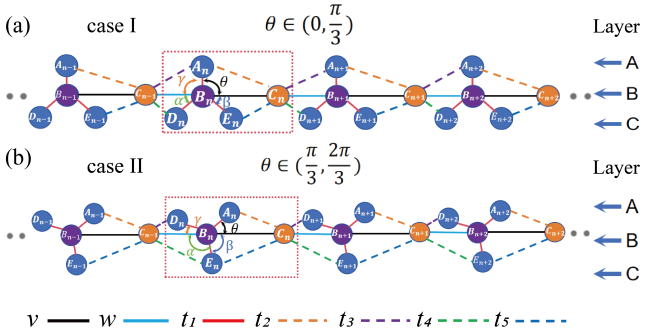

Fig. 1. Schematic of a cluster-doped SSH photonic lattice. The lines represent coupling coefficients, while θ, γ, α, and β denote the angles between the cluster and the SSH substrate lattice. The red dashed box indicates the unit cell. The structural configurations of the system under different ranges of θ are illustrated in panels (a) and (b). (The three layers A, B, and C correspond to the vertical distribution of the lattice.)

quantitative modulation of the coupling between the cluster and the host lattice, thereby enabling control over the localization and robustness of the edge modes. Through numerical simulations of energy spectra, disorder robustness analysis, and beam propagation studies, we demonstrate its dynamic switching capability, which yields distinct transmission characteristics at different rotation angles, providing a practical pathway toward dynamically reconfigurable photonic devices.

Figure 1 illustrates the structure of the model, where the blue lattice sites represent the introduced auxiliary sites. Together with the left lattice of the SSH chain, they form a four-atom unit with a minimum rotation period of $2\pi/3$. Thus, when $\theta \in (0, \pi/3)$ [Fig. 1(a)] and when $\theta \in (\pi/3, 2\pi/3)$ [Fig. 1(b)], the auxiliary sites undergo an up-down flipping, leading to two distinct Hamiltonians. However, the computational results obtained from these two configurations follow the same physical mechanism; the following discussion will focus primarily on the case within the range $\theta \in (\pi/3, 2\pi/3)$. The Hamiltonian corresponding to Case II is given by:

$$H_{II} = \begin{bmatrix} 0 & t_1 & t_2 + t_3 e^{i\vec{k}\cdot\vec{a}} & 0 & 0 \\ t_1 & 0 & v + we^{i\vec{k}\cdot\vec{a}} & t_1 & t_1 \\ t_2 + t_3 e^{-i\vec{k}\cdot\vec{a}} & v + we^{-i\vec{k}\cdot\vec{a}} & 0 & t_4 e^{-i\vec{k}\cdot\vec{a}} & t_5 \\ 0 & t_1 & t_4 e^{i\vec{k}\cdot\vec{a}} & 0 & 0 \\ 0 & t_1 & t_5 & 0 & 0 \end{bmatrix}, \tag{1}$$

here, v and w denote the coupling coefficients between sites B_n and C_n within the backbone of the lattice, while t_1 corresponds to the intra-cluster coupling coefficient connecting the auxiliary sites to the central site. The parameter values used in this work are $v = 1$, $w = 1.5$, and $t_1 = 2$ (with the corresponding interatomic spacing set to $d_v = \pi/2$, $d_w = \pi/3$ and $d_1 = \pi/4$), which place the underlying SSH backbone in the topologically nontrivial regime. The analysis for the topologically trivial case is presented in Supplement 1, Section A. The primitive lattice vector of the unit cell is given by $\vec{a} = (d_v + d_w)\vec{x}$, and $\vec{k}$ denotes the Bloch wave vector. The relationship between the coupling coefficient, coupling length, and waveguide spacing is given by [21]:

$$t_i(\theta) = \frac{\pi}{2l_i(\theta)}, \quad i = 2, 3, 4, 5, \tag{2}$$

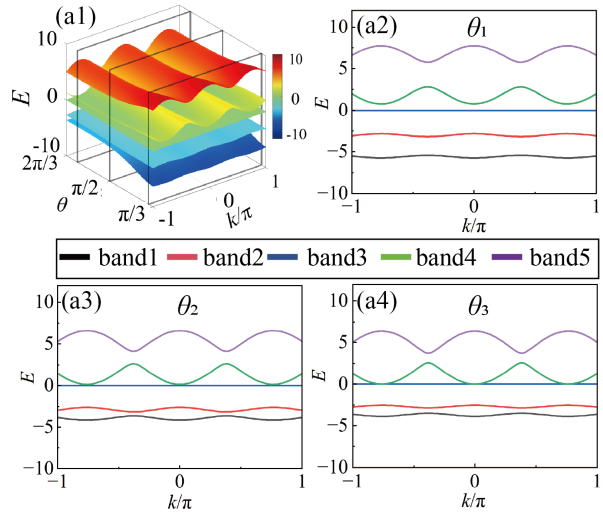

Fig. 2. Schematic of the band structure. (a1) Band evolution as a function of the wave vector k and the rotation angle θ. (a2)–(a4) Corresponding energy band structures at different rotation angles, where (a2) corresponds to $\theta_1 = 7\pi/18$, (a3) to $\theta_2 = \pi/2$, and (a4) to $\theta_3 = 11\pi/18$. Here, $t_1 = 2$, $v = 1$, and $w = 1.5$. The rotation angles used in subsequent analyses correspond to those specified in this section.

here, $l_i(\theta) \approx \pi[1 + \eta_i d_i(\theta)]/(2t_{0,i})$ represents the coupling length, $d_i(\theta)$ denotes the waveguide spacing, while $t_{0,i}$ and η_i are the effective parameters for the i-th channel, whose values depend on the wavelength and the properties of the waveguide material. The expression for $d_i(\theta)$, the derivation of $l_i(\theta)$, and the parameter values are all provided in Supplement 1, Section B.

By computing the Hamiltonian under different rotation angles, we obtain the band structure shown in Fig. 2. It can be observed that the rotation of the cluster significantly alters the original band structure of the SSH lattice. First, the introduction of clusters breaks the inversion symmetry P of the lattice, resulting in the loss of symmetry of all energy bands about $E = 0$. The band gap exhibits a continuous narrowing trend as the rotation angle θ increases, with a rate of change $\partial E/\partial\theta \approx 0.081$. As shown in [Figs. 2(a2)–2(a4)]. Furthermore, local coupling within the cluster induces a strictly flat band near the Γ point. This arises from destructive interference in the wavefunction amplitudes during hopping processes [22]. For calculations and analysis of the flat band, refer to Supplement 1, Section C.

Next, we constructed a finite-sized structural model comprising 20-unit cells. Due to the introduction of clusters, the boundary configurations of the system exhibit two distinct types. Accordingly, we built four types of finite-size models for analysis: double-cluster boundaries, double-atom boundaries, and mixed left(right)-cluster–right(left)-atom boundaries.

As shown in Fig. 3, the boundary structure is crucial in determining the emergence of edge modes. Specifically, [Figs. 3(a1) and 3(a2)] correspond to structures with an integer number of unit cells, while [Figs. 3(a3) and 3(a4)] represent defect structures where a single lattice site has been either added or removed. When the cluster is placed at the left boundary, the left-edge mode consistently appears within the first–second and fourth–fifth band gaps, exhibiting notable modulation with varying angles, as seen in [Figs. 3(b1) and 3(b4)]. In contrast, when the atomic site is at the right boundary, the corresponding edge

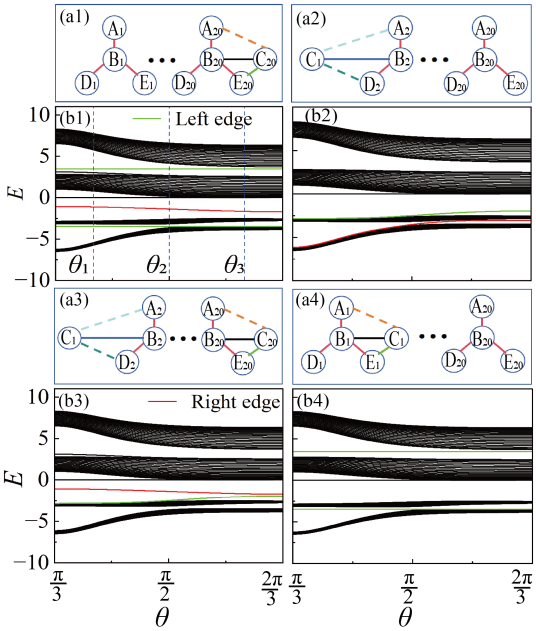

Fig. 3. Energy spectra of the finite-sized system under different boundary conditions. (a1) Mixed left-cluster–right-atom boundaries. (a2) Mixed left-atom–right-cluster boundaries. (a3) Double-atom boundaries. (a4) Double-cluster boundaries. (b1)–(b4) The corresponding energy spectrum diagram.

mode remains localized within the second and third band gaps, showing no sensitivity to changes in θ. On the other hand, when the atomic site is positioned at the left boundary, the edge mode behaves oppositely to the cluster case: as θ increases, the mode detaches from the bulk states and becomes left-localized, as shown in [Figs. 3(b2) and 3(b3)].

Next, we select the left-cluster–right-atom boundary structure [Fig. 3(a1)] for stability verification. The robustness of the edge states is examined by introducing disorder into the system. We apply random disorder to these parameters as follows:

$$t_{1n} = t_1 + d\delta_n, v_n = v + d\delta_n, w_n = w + d\delta_n,\ t_{in} = t_i + d\delta_n, \tag{3}$$

where n denotes the unit cell index, δ_n is uniformly distributed between -1 and 1, and d represents the disorder strength [23]. To ensure generality, we set the random factor δ_n to vary randomly with the unit cell index n, meaning that each unit cell has a distinct random factor.

Figure 4 presents the averaged results from 100 simulations, illustrating the evolution of edge modes under varying disorder strength d for three different angles. All plots share the same initial parameter values: $t_1 = 2, v = 1, w = 1.5$. It is clearly observed that at smaller values of θ, both left and right-edge modes exhibit strong robustness against random disorder. As θ increases, the right-edge mode (red curve) remains stable due to the decisive role of boundary configuration in mode stability. In contrast, the left-edge mode (green curve) shows a pronounced weakening trend with increasing θ. Notably, edge modes within the first and second band gaps revert completely to bulk states at larger values of θ. The analysis and discussion of the introduced potential disorder are provided in Supplement 1, Section D.

Based on the above analysis, we computed the real-space distributions of the edge modes at angles θ_1 and θ_3. Additionally,

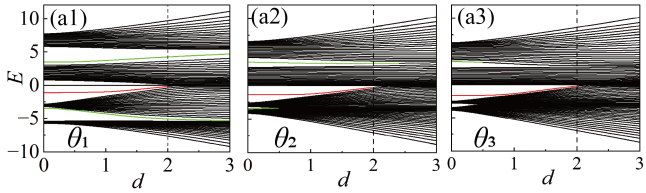

Fig. 4. Effect of introduced disorder on the robustness of edge modes at different angles ($\theta_1, \theta_2, \theta_3$). (a1)–(a3) The boundary configuration is of the left-cluster-right-lattice type.

the Inverse Participation Ratio (IPR) was introduced, defined as $\mathrm{IPR}_m = \sum_i |\psi_m(i)|^4$ [24], to quantitatively characterize the degree of localization of the edge modes, where $\psi_m(i)$ denotes the normalized wave function. For this finite-sized system consisting of 100 lattice sites, we set the IPR threshold to 0.1. This criterion is approximately ten times the IPR of bulk states and serves to distinguish localized modes from extended ones.

As shown in Fig. 5, the mode profiles and wavefunction distributions of the edge modes at $\theta_1 = 7\pi/18$ and $\theta_3 = 11\pi/18$ are plotted, along with the corresponding Gaussian beam propagation diagrams. As clearly observed, at larger rotation angles, shown in [Figs. 5(a1)–5(a3)], the right-edge mode remains localized—a consequence of its boundary configuration—while the edge modes within the fourth and fifth band gaps exhibit significantly weakened localization, transitioning into a weakly localized regime. In contrast, the edge modes originally located in the first and second band gaps completely degenerate into bulk states. On the other hand, at smaller angles, as depicted in [Figs. 5(b1)–5(b3)], both left and right boundaries demonstrate strong localization characteristics (IPR > 0.1). The underlying mechanism stems from the modulation of coupling coefficients between the cluster and the host lattice via the rotation angle—this tuning approach constructs a deep potential well in the small-angle regime, thereby forming highly localized and stable edge modes.

The incident field of the Gaussian beam is given by [25]:

$$E(z=0) = a_1 e^{-\left(\frac{m-m_1}{\omega}\right)^2 + ik_0 m} + a_2 e^{-\left(\frac{m-m_2}{\omega}\right)^2 + ik_0 m} + a_3 e^{-\left(\frac{m-m_3}{\omega}\right)^2 + ik_0 m}, \tag{4}$$

here, $a_{(1,2,3)}$ represents the excitation amplitudes, and $m_{(1,2,3)}$ denotes the indices of the lattice sites being excited. When exciting the left boundary mode [Figs. 5(a3), 5(b1), and 5(b3)], $m_{(1,2,3)}$ corresponds to lattice sites A_1, B_1, and D_1, while $a_{(1,2,3)}$ gives the amplitudes and phases at these sites. When exciting the right boundary mode [Figs. 5(a2) and 5(b2)], $m_{(1,2,3)}$ corresponds to lattice sites A_{20}, C_{20}, and E_{20}, and $a_{(1,2,3)}$ provides the amplitudes and phases at these sites. The parameter m refers to the position index across the 100 lattice points, w is the beam width, and k_0 is the initial wave vector.

Through transmission profiles, we further verify the modulation effect of the angle on the robustness of edge modes. Specifically, the propagation diagrams in [Figs. 5(a4)–5(a6)] and [Figs. 5(b4)–5(b6)] correspond one-to-one with the wave function distributions shown in [Figs. 5(a1)–5(a3)] and [Figs. 5(b1)–5(b3)], respectively. The excitation amplitudes and phases are determined by the wave function distributions and are distinct from one another. At larger angles, as illustrated in [Figs. 5(a4)–5(a6)], the edge modes corresponding to the cluster-terminated boundary exhibit reduced localization or

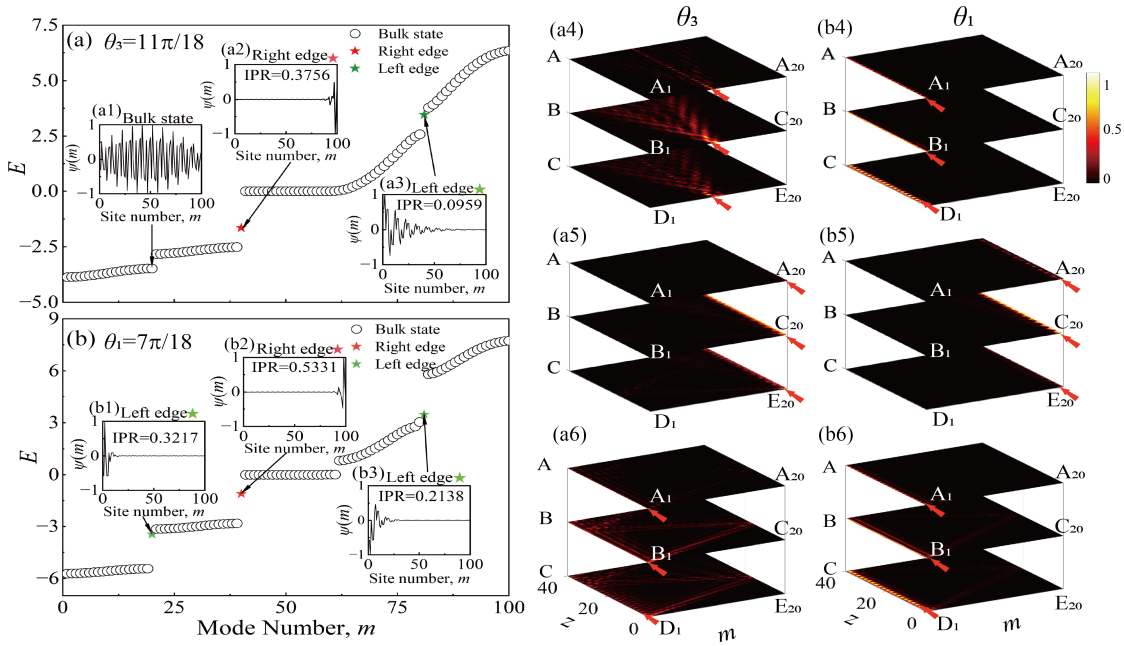

Fig. 5. Mode distributions at different cluster rotation angles. (a1)–(a3) Real-space distributions of mode 20 (bulk state), mode 40 (right-edge state), and mode 81 (left-edge state) at θ_3. (b1)–(b3) Real-space distributions of mode 20 (bulk state), mode 40 (right-edge state), and mode 81 (left-edge state) at θ_1. (a4)–(a6) Excitation transport diagrams for modes 20, 40, and 81 at θ_3. (b4)–(b6) Excitation transport diagrams for modes 20, 40, and 81 at θ_1. Its structural distribution is consistent with that shown in Fig. 3(a1).

even degenerate into bulk states, resulting in higher transmission losses. In contrast, at smaller angles, as shown in [Figs. 5(b4)–5(b6)], the cluster-terminated boundary supports highly localized and stable transmission. This method of generating robust edge states does not rely on lattice symmetry but achieves controllable boundary robustness through angular tuning, offering an innovative strategy for fabricating tunable photonic devices. Based on these findings, a feasible experimental scheme is outlined in Supplement 1, Section E.

In summary, this study establishes a novel geometry-driven paradigm that successfully achieves robust boundary states in photonic lattices. We demonstrate that the cluster rotation angle θ, as a continuously tunable physical parameter, can precisely modulate the coupling strength between the cluster and the host lattice. This directly controls the depth and profile of the boundary potential well, thereby determining the degree of localization and the disorder resistance of the edge modes. Furthermore, our work reveals the decisive regulatory role of the boundary geometry: boundaries terminated by a single atomic site support strongly localized edge modes whose stability is largely insensitive to variations in θ, whereas boundaries terminated by a cluster produce edge modes that are highly sensitive to changes in θ. This finding clearly underscores the geometric origin of the robustness of boundary states, offering a new physical foundation and a practical pathway for designing on-demand reconfigurable photonic devices.

Funding. National Natural Science Foundation of China (12174307).

Disclosures. The authors declare no conflicts of interest.

Data availability. No data were generated or analyzed in the presented research.

Supplemental document. See Supplement 1 for supporting content.

REFERENCES

1. H. Huang, Z. Du, K. Liao, *et al.*, Sci. Adv. **11**, eadw7198 (2025).
2. A. Zannotti, J. M. Vasiljević, D. V. Timotijević, *et al.*, Opt. Lett. **44**, 1592 (2019).
3. S. Stützer, Y. Plotnik, Y. Lumer, *et al.*, Nature **560**, 461 (2018).
4. A. Fritzsche, T. Biesenthal, L. J. Maczewsky, *et al.*, Nat. Mater. **23**, 377 (2024).
5. T. Tang, M. R. Belić, H. Zhong, *et al.*, Opt. Lett. **49**, 4110 (2024).
6. R. A. Vicencio Poblete, Adv. Physics: X **6**, 1878057 (2021).
7. X. Lu, A. McClung, and K. Srinivasan, Nat. Photonics **16**, 66 (2022).
8. X.-D. Chen, F.-L. Zhao, M. Chen, *et al.*, Phys. Rev. B **96**, 020202 (2017).
9. Y. Zeng, U. Chattopadhyay, B. Zhu, *et al.*, Nature **578**, 246 (2020).
10. Z. Lan, M. L. Chen, F. Gao, *et al.*, Rev. Phys. **9**, 100076 (2022).
11. M. Li, N. Han, J. Song, *et al.*, Phys. Rev. B **106**, 075301 (2022).
12. W. P. Su, J. R. Schrieffer, and A. J. Heeger, Phys. Rev. Lett. **42**, 1698 (1979).
13. N. Malkova, I. Hromada, X. Wang, *et al.*, Opt. Lett. **34**, 1633 (2009).
14. M. C. Rechtsman, J. M. Zeuner, Y. Plotnik, *et al.*, Opt. Lett. **496**, 196 (2013).
15. Y. V. Kartashov, Chaos Soliton Fract. **185**, 115188 (2024).
16. H. X. Wang, L. Liang, B. Jiang, *et al.*, Photonics Res. **9**, 1854 (2021).
17. M. Ezawa, Phys. Rev. Lett. **120**, 026801 (2018).
18. T. Liu, K. Bai, Y. Zhang, *et al.*, Light. Sci. Appl. **13**, 69 (2024).
19. W. Yan, R. Chen, W. Liu, *et al.*, Laser Photonics Rev. **19**, 2402126 (2025).
20. R. Chen, W. Yan, W. Liu, *et al.*, Sci. Bull. **70**, 1605 (2025).
21. F. Lederer, G. I. Stegeman, D. N. Christodoulides, *et al.*, Phys. Rep. **463**, 1 (2008).
22. J. W. Rhim and B. J. Yang, Phys. Rev. B **99**, 045107 (2019).
23. V. M. M. Alvarez and M. D. Coutinho-Filho, Phys. Rev. A **99**, 013833 (2019).
24. F. Evers and A. Mirlin, Rev. Mod. Phys. **80**, 1355 (2008).
25. J. Yang, Y. Wang, Y. Lin, *et al.*, Opt. Lett. **49**, 266 (2024).